ROYAL SOCIETY OF CHEMISTRY

PAPER

Probing dynamic covalent chemistry in a 2D boroxine framework by *in situ* near-ambient pressure X-ray photoelectron spectroscopy†

Paul Leidinger, [ID] [a] Mirco Panighel, [ID] [b] Virginia Pérez Dieste, [c] Ignacio J. Villar-Garcia, [ID] [c] Pablo Vezzoni, [ID] [d] Felix Haag, [d] Johannes V. Barth, [d] Francesco Allegretti, [d] Sebastian Günther [ID] [a] and Laerte L. Patera [ID] ⋆[a,e]

Dynamic covalent chemistry is a powerful approach to design covalent organic frameworks, where high crystallinity is achieved through reversible bond formation. Here, we exploit near-ambient pressure X-ray photoelectron spectroscopy to elucidate the reversible formation of a two-dimensional boroxine frame-work. By *in situ* mapping the pressure–temperature parameter space, we identify the regions where the rates of the condensation and hydrolysis reactions become dominant, being the key to enable the thermodynamically controlled growth of crystalline frameworks.

aDepartment of Chemistry and Catalysis Research Center, Technical University of Munich, 85748 Garching, Germany
bCNR-IOM, Laboratorio TASC, 34149 Trieste, Italy
cCELLS-ALBA Synchrotron Radiation Facility, 08290 Cerdanyola del Valles, Spain
dPhysics Department E20, Technical University of Munich, 85748 Garching, Germany
eInstitute of Physical Chemistry, University of Innsbruck, 6020 Innsbruck, Austria.
E-mail: laerte.patera@uibk.ac.at
†Electronic supplementary information (ESI) available. See DOI: https://doi.org/10.1039/d2nr04949j

Dr. Laerte L. Patera is an Assistant Professor at the University of Innsbruck (Austria). He received his PhD in Nanotechnology from the University of Trieste (Italy) in 2016 and worked as a postdoctoral researcher at the University of Regensburg (Germany) from 2016 to 2019. In 2020, he started his independent career at the Technical University of Munich (Germany). He was awarded the Gustav Hertz Prize

Laerte L. Patera

of the German Physical Society (2019) and an ERC Starting Grant (2022). His research is focused on the synthesis and imaging of two-dimensional covalent organic frameworks for energy conversion.

Introduction

Covalent organic frameworks (COFs) are materials formed by the covalent linkage of organic building blocks to create periodic structures with predefined topologies.[1] COFs feature reticular structures with an ordered organic backbone, whose flexible choice allows tuning the structural and optoelectronic properties.[2,3] While 3D-COFs have covalent bonds extended through the entire network,[4] 2D-COFs are restrained to in-plane bonds, placing them in the field of 2D materials. Among the variety of possible coupling schemes,[5] covalent bonding is typically achieved through condensation reactions, yielding water as a by-product.[6,7] Recently, the formation of extended 2D-COFs has been demonstrated by on-surface synthesis, which exploits atomically flat surfaces as templates to restrict and guide reaction pathways in two dimensions.[7–11] However, on-surface synthesis of atomically thin COFs based on condensation reactions under ultra-high vacuum (UHV) conditions typically results in a low degree of crystallinity.[12–18] This issue is related to the irreversibility of the covalent bond formation, as the water by-product from the condensation reaction is promptly pumped away. In contrast, applying the dynamic covalent chemistry strategy, the addition of water enables a certain rate of backreaction, providing a mechanism for error correction and, thus, facilitating the formation of a thermodynamically most stable crystalline structure.[1,6,19–23] For the case of boronic acid condensation, where three boronic acid groups form a six-membered boroxine ring (B_3O_3),[24,25] thermodynamically controlled crystallization has been reported by introducing water vapor during the reaction.[19,20] However, the water partial pressure (p_{H_2O}) required for the crystallization

could not be determined.[21] A recent study exploited *in situ* scanning tunnelling microscopy (STM) at the solid–liquid interface to quantitatively extract information on crystallization parameters, such as critical nucleus size, nucleation and growth rate.[26] Despite the unprecedented fundamental understanding provided by such a microscopic approach, the experiments were performed at room temperature only and in a limited humidity range. As p_{H_2O} is a key parameter to determine the chemical equilibrium of the system, systematic studies under different experimental conditions (*i.e.* p_{H_2O} and temperature T) are required to identify the fundamental thermodynamic reaction values and the parameter space where highly crystalline 2D-COFs can be achieved.[27]

Recent developments in surface-science techniques capable of working at elevated pressures offer an appealing approach for novel *in situ* investigations of chemical reactions occurring at surfaces.[28–33] In particular, differentially pumped electron optics allowed pushing X-ray Photoelectron Spectroscopy (XPS) up to ambient pressures. In this way, surface species can be monitored with elemental and chemical specificity under conditions closer to those present in industrial chemical reactors.[28,34–40] This approach has successfully been exploited to probe atomic scale mechanisms governing the growth of 2D materials in realistic environments.[41–45]

Here, we studied the polymerization and hydrolysis of an atomically thin boroxine (B_3O_3) framework on Au(111). By controlling p_{H_2O} and T, the chemical equilibrium could be tuned, leading to reversible formation or dissolution of the framework. By exploiting near-ambient pressure X-ray photoelectron spectroscopy (NAP-XPS), we monitored *in situ* the evolution of the surface species and shed light on the parameter space governing the thermodynamically controlled bond formation in boroxine-based 2D-COFs.

Results and discussion

As a model system to study the reversible condensation of boronic acid, we focused on a 2D boroxine framework resulting from the cyclocondensation of tetrahydroxydiboron (THDB) on Au(111),[46] as shown in Scheme 1. This reaction has been previously studied, showing that polycondensation leads to an atomically thin amorphous film composed of covalently

connected boroxine rings.[46] The condensation reaction of boronic acid is exothermic:

$$3THDB_{ad} \rightarrow 2B_3O_3 + 6H_2O \uparrow$$
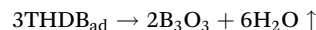
and under UHV conditions the produced H_2O molecules are pumped away without re-adsorbing on the Au(111) surface (as indicated by the up arrow on the right side of the equation). By increasing the water partial pressure (p_{H_2O}), the reaction can be made reversible:

$$3THDB_{ad} \rightleftharpoons 2B_3O_3 + 6H_2O \uparrow\downarrow$$
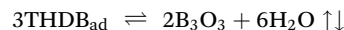
Considering also the possible THDB desorption from the surface, the overall reaction can be written as:

$$3THDB_g \uparrow\leftarrow 3\ THDB_{ad} \rightleftharpoons 2B_3O_3 + 6H_2O \uparrow\downarrow$$

In this work we show that by tuning p_{H_2O} and T, the rate of the backreaction (r_{hydr}) can be controlled, enabling reversible covalent bond formation. In this way it is possible to identify the conditions which enable dynamic covalent chemistry to occur in a 2D boroxine framework.

THDB molecules were sublimated on the Au(111) surface kept at different Ts, ranging from 200 K to 393 K. The temperature stability of the THDB precursor has been determined through temperature-programmed desorption (TPD) experiments in UHV. Fig. 1a shows a TPD spectrum for the m/z value
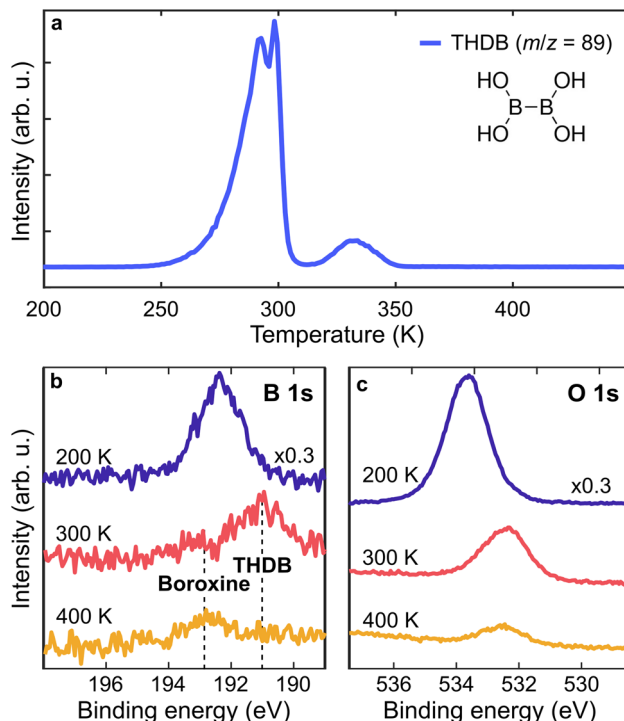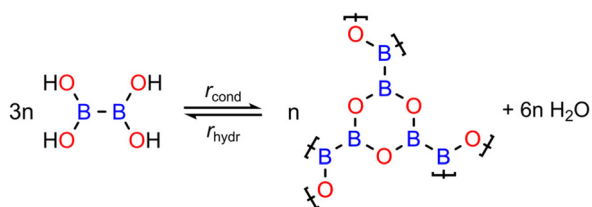

Fig. 1 On-surface formation of the boroxine framework in UHV. (a) TPD measurement for the intact THDB molecule (m/z = 89 amu, linear heating rate of 1 K s^{-1}). (b and c) B 1s and O 1s spectra of THDB/Au(111) after initial multilayer deposition at 200 K (blue), and after annealing to 300 K (red) and 400 K (orange), respectively. Photon energy = 1253.6 eV.

Scheme 1 Reversible condensation reaction of tetrahydroxydiboron (THDB) leading to a 2-dimensional boroxine (B_3O_3) framework. The rates of condensation (r_{cond}) and hydrolysis (r_{hydr}) are indicated.

of 89 amu corresponding to the intact THDB molecule. A multilayer film was obtained by evaporating THDB on Au(111) kept at 200 K. Multilayer desorption sets in at ≈260 K, peaking at ≈290 K, while the peak at ≈300 K is attributed to the desorption of the second adsorbed layer.[47] Further desorption is observed at ≈330 K, indicating partial desorption of the monolayer film.

To identify the surface species we acquired X-ray Photoelectron (XP) spectra of the B 1s and O 1s core levels after annealing a multilayer film to 200, 300 and 400 K (Fig. 1b and c). The B 1s and O 1s spectra acquired at 200 K are attributed to the multilayer THDB regime. The pronounced intensity reduction upon annealing to 300 K indicates the desorption of the multilayer. The B 1s spectrum exhibits a shift from ≈192.3 eV to ≈191.2 eV (due to the formation of a molecular monolayer), together with the formation of a small component at ≈192.8 eV. Stredansky *et al.* attributed the latter species to the boroxine framework,[46] while a larger peak at ≈191.2 eV is here assigned to the adsorbed, unreacted THDB monomers. Upon annealing to 400 K, a complete vanishing of the monomer species is accompanied by enhanced growth of the boroxine component. Overall, the combined TPD and XPS results show that the cyclocondensation of the THDB monolayer to the boroxine framework in UHV already (slowly) occurs at 300 K and is completed at 400 K, accompanied by the desorption of the THDB monomers. While the O 1s spectra exhibit a clear energy shift once annealed from 200 K to 300 K (multilayer to monolayer transition), further annealing to 400 K does not lead to a pronounced change in the binding energy (≈200 meV), making the O 1s core level not sensitive enough to probe the transition from the THDB monolayer to the boroxine framework. Therefore, in the following we focus mainly on the changes in the B 1s spectra.

After having clarified the temperature evolution and stability of the THDB precursors and the conditions required for the formation of the boroxine framework on Au(111) under UHV conditions, we focus on the effect of p_{H_2O} on the presence of the boroxine framework. For this purpose, we performed near-ambient pressure XPS (NAP-XPS). Fig. 2a and b show the B 1s and O 1s XP spectra acquired at $T = 323$ K for a boroxine framework under different p_{H_2O} values (the corresponding survey spectra are shown in Fig. SI1†). By increasing p_{H_2O} up to 6×10^{-3} mbar no change can be detected in the XP spectra. A slight decrease in peak intensity can be observed at $p_{H_2O} = 0.1$ mbar (see the time-resolved B 1s spectra in Fig. SI2†), while at 1 mbar the boron and most of the oxygen signals vanish. This is confirmed also by the spectra acquired after evacuation of the cell ($p_{H_2O} < 1 \times 10^{-6}$ mbar). Here, the residual oxygen signal is attributed to surface contamination due to the water-induced displacement of oxygen-containing carbonaceous species from the internal chamber walls,[48,49] as suggested also by the C 1s spectra shown in Fig. SI3.† As hydrolysis of boroxine can already occur at low temperatures,[50] the behaviour shown in Fig. 2a and b can be rationalized as a water-induced dissolution of the boroxine framework ($r_{hydr} > r_{cond}$, where r_{cond} and r_{hydr} are the rates of condensation and
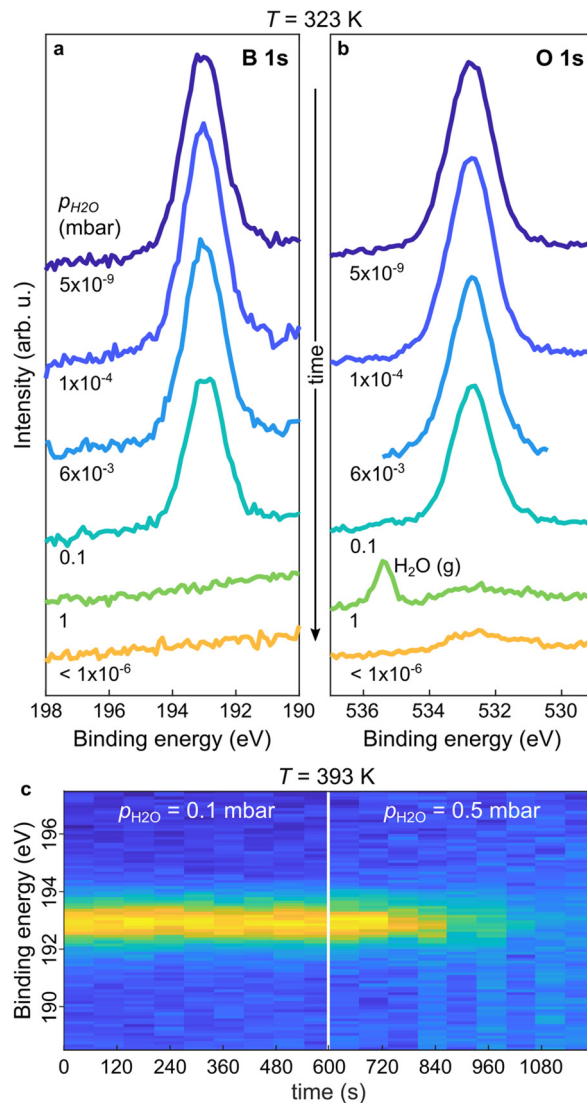

Fig. 2 *In situ* NAP-XPS characterization of hydrolysis in the boroxine framework upon water vapor exposure. (a and b) B 1s and O 1s spectra of the boroxine framework on Au(111) upon sequential exposure to increasing p_{H_2O} (shown in shades of blue and green) and after cell evacuation (indicated in orange) at $T = 323$ K. The water gas-phase peak, $H_2O(g)$, is indicated. (c) Contour plot of B 1s spectra acquired during exposure of the boroxine framework to water vapor pressures at $T = 393$ K, with p_{H_2O} increased from 0.1 to 0.5 mbar after 600 s. Photon energy = 650 eV.

hydrolysis reactions), for p_{H_2O} as low as 0.1 mbar. In particular, given that the THDB monomers are not stable on the surface above about 320 K (see Fig. 1a), the hydrolysis of the framework leads to instantaneous desorption of the hydrolysed THDB molecules ($r_{des} \gg r_{hydr} - r_{cond}$, where r_{des} is the rate of THDB desorption).

To understand the role of p_{H_2O} under conditions typically used for the crystallization of boroxine-based COFs, we monitored the time evolution of the boron species at higher temperatures.[20,21,51] Fig. 2c shows a time series of B 1s spectra acquired during water exposure at $T = 393$ K. At $p_{H_2O} =$

0.1 mbar the boroxine XPS intensity is constant. In contrast, rising p_{H_2O} to 0.5 mbar results in a rapid decrease of the signal, completely vanishing after 300 s. This suggests that at T = 393 K and p_{H_2O} = 0.1 mbar, the boroxine hydrolysis rate is still smaller than the one for THDB condensation ($r_{hydr} < r_{cond}$), but increasing p_{H_2O} to 0.5 mbar initiates this reaction path ($r_{hydr} > r_{cond}$), combined with the immediate desorption of the formed monomer THDB species ($r_{des} \gg r_{hydr} - r_{cond}$).

As the hydrolysed molecules were not detected at T = 393 K, the spectra in Fig. 2c do not represent direct proof of the reversible condensation reaction of the boroxine framework. Therefore, we carried out further *in situ* studies at T = 300 K, at which the THDB monomers are stable on the gold surface and should coexist with the condensed species (see Fig. 1). Fig. 3a and b show the B 1s and O 1s spectra acquired at 300 K. Given that at very low p_{H_2O} values the condensation reaction of boronic acid is exothermic ($r_{cond} > 0$, $r_{hydr} \approx 0$),[18,26] a fraction of the THDB molecules forms boroxine species ($r_{hydr} < r_{cond}$) upon deposition at 300 K. This is evident from the lineshape of the B 1s spectrum acquired at p_{H_2O} = 5 × 10^{-9} mbar (Fig. 3a), exhibiting two components, corresponding to the intact THDB molecules (red) and COF boroxine framework (blue). At p_{H_2O} = 7 × 10^{-3} mbar, partial elimination of THDB is indicated by the decrease in the absolute intensity of the XPS component (see Fig. 3c). This is accompanied by a reduction of the boroxine peak intensity, revealing a significant rate of hydrolysis ($r_{hydr} > r_{cond}$). As the THDB to boroxine ratio decreases (see Fig. 3c) the THDB desorption rate (r_{des}) is larger than that of boroxine dissolution, revealing that at T = 300 K and p_{H_2O} = 7 × 10^{-3} mbar, $r_{des} > r_{hydr} - r_{cond}$. The adsorption of water due to the polar nature of the boronic acid groups and the presence of oxygen-containing contaminations (see Fig. SI3†), in addition to the close components corresponding to the THDB and boroxine frameworks, complicate the quantitative interpretation of the O 1s spectra. At p_{H_2O} values of 0.1 and 0.5 mbar, the ratio of THDB to boroxine rises, due to a higher hydrolysis rate. Indeed, time-resolved spectra (see Fig. SI4 and 5†) acquired at p_{H_2O} = 0.5 mbar show that boroxine hydrolysis proceeds faster than THDB desorption ($r_{hydr} - r_{cond} > r_{des}$). Instead, upon subsequent evacuation of the reaction cell ($p_{H_2O} < 1 × 10^{-6}$ mbar), the THDB to boroxine ratio decreases ($r_{hydr} < r_{cond}$), due to the suppression of the water-induced hydrolysis of boroxine ($r_{hydr} \approx 0$), and the absolute intensity of the boroxine component rises, indicating full control over the hydrolysis process through the adjustment of p_{H_2O}. Notably, this represents the first *in situ* direct observation of dynamic covalent chemistry in 2D-COFs.

Aiming at achieving crystalline COFs, it is pivotal to identify the parameter space where the rates of the reaction and back-reaction (almost) equalize. Fig. 4 shows a pressure–temperature diagram of the reversible condensation reaction obtained from the presented datasets (Fig. 2 and 3). While at a given T, it is difficult to determine the exact p_{H_2O} value where r_{hydr} and r_{cond} are equal (given the limited measurement time), we defined upper and lower boundaries, where significant and no hydrolysis, respectively, is observed, as marked
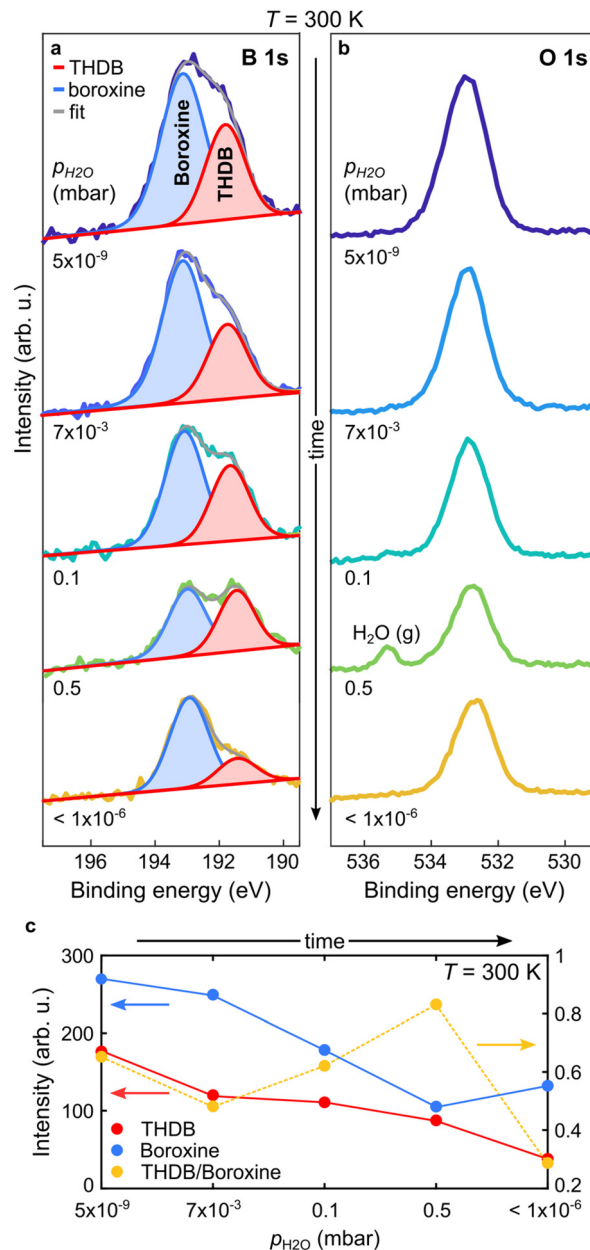

Fig. 3 *In situ* NAP-XPS characterization of a mixed boroxine and THDB monolayer upon water vapor exposure. (a and b) B 1s and O 1s spectra acquired at T = 300 K upon a sequential increase of p_{H_2O} and after cell evacuation. Photon energy = 650 eV. (a) Individual components obtained by the fitting procedure are superimposed as solid peaks. (c) Absolute intensities of the two B 1s components of panel (a) and their intensity ratio are plotted *versus* p_{H_2O}.

in Fig. 4 (see Methods). Exploiting the diagram, a crystalline framework could be, in principle, obtained by using a condition where the rate of condensation is slightly larger than the rate of hydrolysis. However, in this specific case, the loss of reactant THDB molecules hinders the formation of a crystalline 2D boroxine framework. In fact, the conditions favouring bond reversibility coincide with the desorption of the hydrolysed molecules.
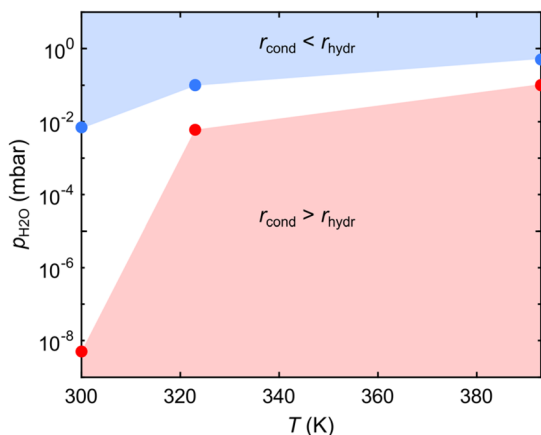
Fig. 4 Pressure–temperature diagram of the reversible condensation reaction of tetrahydroxydiboron (THDB) leading to a 2D boroxine framework. The regions where the rates of the condensation (r_{cond}) and hydrolysis (r_{hydr}) reactions become dominant are indicated in red and blue, respectively.

The effect of even higher p_{H_2O} (>1 mbar) was investigated *ex situ* by means of STM imaging (Fig. 5). The region imaged in Fig. 5a displays four ascending Au(111) terraces (from left to right), separated by monoatomic steps. Each terrace is partly covered by a network phase which resembles the boroxine phase and which appears slightly higher than the supporting Au terrace in the STM image. While the incomplete filling is readily observed in the large overview, the zoomed area shown in the inset of Fig. 5a proves the porous and amor-
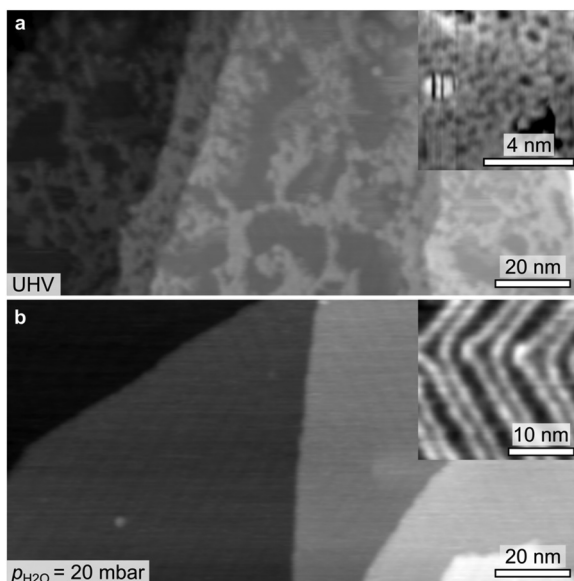
phous nature of the network structure, which has been previously reported.[46] Exposure of the boroxine framework to 20 mbar of water vapor at 300 K for 15 minutes results in the complete hydrolysis of the boroxine framework and in the desorption of the entire THDB monolayer (Fig. 5b). As a result, flat Au(111) terraces are observed when imaging the surface after water exposure by STM as shown in Fig. 5b, where the characteristic herringbone reconstruction of the Au(111) surface is clearly resolved.[52]

Conclusions

We exploited NAP-XPS to enable *in situ* observations of dynamic covalent chemistry in 2D-COFs, in particular for the case of the polymerization and hydrolysis of an atomically thin boroxine (B_3O_3) framework on Au(111). By controlling the sample temperature and the water partial pressure in the reaction chamber, the shift of the prevalent surface species can be tracked in real time. While at $T = 300$ K, hydrolysis of the boroxine network is observed already at $p_{H_2O} = 7 \times 10^{-3}$ mbar, under typical conditions for 2D-COF growth ($T = 393$ K), a p_{H_2O} of ≈0.5 mbar is needed to induce a shift in equilibrium towards the reactant monomers. By mapping the pressure–temperature parameter space, we identified the regions where the rates of the condensation and hydrolysis reactions become dominant. The synthesis of a crystalline boroxine framework has been hindered by the competing desorption of the THDB precursors occurring upon hydrolysis of the network, as confirmed by STM. Importantly, we have shown that reversible bond formation in 2D boroxine frameworks occurs in the (sub-)mbar pressure regime, enabling the use of current NAP-XPS analysers[36,53] for the *in situ* investigation of dynamic covalent chemistry. The presented approach can be extended to a large variety of 2D-COFs. Furthermore, in combination with rigorous analysis,[27] it opens the possibility of precisely determining relevant parameters, such as the kinetic barriers for reversible reactions, as well as the Gibbs free energy ruling the dynamic covalent bond formation.

Methods

THDB molecules (purity: 95%) were purchased from Sigma Aldrich and sublimated on the Au(111) surface from a Knudsen cell kept at a temperature of about 350 K.

UHV-XPS and TPD experiments were performed in a home-built UHV chamber. The XPS measurements were carried out using the non-monochromated Mg Kα line ($h\nu = 1253.6$ eV) from a standard X-ray tube and a SPECS Phoibos 100 CCD hemispherical analyser combined with a PCO pixelfly camera, with an overall energy resolution of ≈900 meV. The binding energies of all XP spectra were calibrated against the Au $4f_{7/2}$ core level of the Au(111) substrate at a binding energy of 84.00 eV. The TPD measurements were performed with a quadrupole mass spectrometer mounted behind a Feulner cap.[54] As the

Fig. 5 STM images acquired at $T = 300$ K after (a) on-surface synthesis of the boroxine framework on Au(111) at $T = 393$ K and (b) after exposure to water vapor at 20 mbar at $T = 300$ K for 15 minutes. (a) Inset: a molecular-resolved image of the disordered boroxine framework. (b) Inset: zoom on a flat terrace, showing the herringbone reconstruction of the Au(111) surface. (a) $V = 0.55$ V; $I = 0.8$ nA. (b) $V = 0.28$ V; $I = 2$ nA.

poor signal to noise ratio of the B 1s spectra hinders a quantitative estimation of the surface coverage, no fit is presented for the B 1s spectra shown in Fig. 1b.

The NAP-XPS experiments were performed at the NAPP station of the CIRCE beamline of the ALBA synchrotron (Barcelona, Spain).[55] Au/mica films have been used as a substrate. Several sputtering (1 keV, Ar^+) and annealing (623–673 K) cycles were performed in the preparation chamber. THDB molecules were evaporated in a dedicated chamber. After transfer to the analysis chamber, the sample cleanliness was checked at a sample temperature of 300 K. B 1s, C 1s, Au 4f and O 1s core level spectra were recorded at a photon energy of 650 eV, with an overall energy resolution of ≈ 200 meV. Carbon contamination was detected in the XP spectra acquired immediately after THDB evaporation, as a C 1s component at 284.0 eV, and attributed to the incomplete outgassing of the organic powder. The binding energies of all XP spectra were calibrated against the Au $4f_{7/2}$ core level of the Au(111) substrate at a binding energy of 84.00 eV. The analyser axis is at 54.7° with respect to the incident X-ray beam. The pressure in the cell was measured with a VACOM BARION passive hot cathode ionization gauge for pressures up to 10^{-3} mbar and with a Type 121A MKS Baratron Absolute Pressure Transducer for higher pressures. Since hot ion-gauge filaments have been reported to facilitate the formation of radicals due to water cracking,[49] most of the experiments were performed with the hot-ion gauge filament turned off. Instead, for the spectra acquired at $p_{H_2O} = 1 \times 10^{-4}$ mbar (see Fig. 2a and b) the hot ion-gauge was used. However, no increase in the oxygen/boron peak ratio was observed compared to the one obtained for $p_{H_2O} = 5 \times 10^{-9}$ mbar, indicating a negligible contamination effect. We observed that the X-ray beam increases the rates of polymerization and hydrolysis (depending on the experimental conditions).[56] For this reason, the X-ray beam intensity was reduced by about a factor of 100 with respect to the standard operating conditions of the beamline, by detuning the undulator. As a result, a beam size of 50×100 μm^2 was used. This resulted in a negligible beam effect over the acquisition time of a spectrum (about 120 s). Measurements have been performed by raster-scanning the sample surface with a step size of 300 μm, allowing for the acquisition of each spectrum on a fresh sample spot. The B 1s core-level spectra were fitted with symmetric Voigt functions and a linear background. The Lorentzian width was constrained to 500 meV during the fit, while the Gaussian width was not constrained, resulting in an overall full width half maximum (FWHM) of 1.4–1.6 eV. The B 1s binding energies were not strictly constrained to account for small shifts due to the interaction with water molecules. Errors arising from the fitting procedure are negligible. The pressure–temperature diagram in Fig. 4 has been constructed from a series of three experiments performed at $T = 300$, 323 and 393 K, where p_{H_2O} has been stepwise increased. For each experiment, we marked the highest p_{H_2O} value at which the boroxine intensity in the B 1s spectra was constant for at least 600 s (red points) and the lowest p_{H_2O} value at which a time-dependent decrease of the signal could be detected (blue points).

STM experiments were performed at 300 K in a UHV chamber ($p = 5 \times 10^{-10}$ mbar) that hosts a high-temperature scanning tunnelling microscope (SPECS Aarhus 150 HT-NAP). Au(111) single-crystal samples were cleaned by several sputtering (Ar^+, 1.5 keV) and annealing (673 K) cycles. Images were acquired in the constant current mode, with the bias voltage applied to the sample and the tip at the ground. Pt/Ir tips were used for imaging. Water vapor exposure for the STM experiments was done in the STM load lock at room temperature. The sample was then directly transfered to the STM chamber without breaking the vacuum.

Conflicts of interest

There are no conflicts to declare.

Acknowledgements

References

1 A. P. Cote, A. I. Benin, N. W. Ockwig, M. O'Keeffe, A. J. Matzger and O. M. Yaghi, *Science*, 2005, **310**, 1166–1170.

2 S. Lin, C. S. Diercks, Y.-B. Zhang, N. Kornienko, E. M. Nichols, Y. Zhao, A. R. Paris, D. Kim, P. Yang, O. M. Yaghi and C. J. Chang, *Science*, 2015, **349**, 1208–1213.

3 M. Lu, J. Liu, Q. Li, M. Zhang, M. Liu, J.-L. Wang, D.-Q. Yuan and Y.-Q. Lan, *Angew. Chem.*, 2019, **131**, 12522–12527.

4 R. Zhu, J. Ding, L. Jin and H. Pang, *Coord. Chem. Rev.*, 2019, **389**, 119–140.

5 L. Grill and S. Hecht, *Nat. Chem.*, 2020, **12**, 115–130.

6 N. Huang, P. Wang and D. Jiang, *Nat. Rev. Mater.*, 2016, **1**, 16068.

7 D. Cui, D. F. Perepichka, J. M. MacLeod and F. Rosei, *Chem. Soc. Rev.*, 2020, **49**, 2020–2038.

8 J. Cai, P. Ruffieux, R. Jaafar, M. Bieri, T. Braun, S. Blankenburg, M. Muoth, A. P. Seitsonen, M. Saleh, X. Feng, K. Müllen and R. Fasel, *Nature*, 2010, **466**, 470–473.

9 Y.-C. Chen, T. Cao, C. Chen, Z. Pedramrazi, D. Haberer, D. G. De Oteyza, F. R. Fischer, S. G. Louie and M. F. Crommie, *Nat. Nanotechnol.*, 2015, **10**, 156–160.

10 M. Bieri, M. T. Nguyen, O. Gröning, J. Cai, M. Treier, K. Aït-Mansour, P. Ruffieux, C. A. Pignedoli, D. Passerone, M. Kastler, K. Müllen and R. Fasel, *J. Am. Chem. Soc.*, 2010, **132**, 16669–16676.

11 S. Clair and D. G. de Oteyza, *Chem. Rev.*, 2019, **119**, 4717–4776.

12 T. Joshi, C. Chen, H. Li, C. S. Diercks, G. Wang, P. J. Waller, H. Li, J. L. Bredas, O. M. Yaghi and M. F. Crommie, *Adv. Mater.*, 2019, **31**, 6–11.

13 C. Chen, T. Joshi, H. Li, A. D. Chavez, Z. Pedramrazi, P. N. Liu, H. Li, W. R. Dichtel, J. L. Bredas and M. F. Crommie, *ACS Nano*, 2018, **12**, 385–391.

14 D. J. Rizzo, Q. Dai, C. Bronner, G. Veber, B. J. Smith, M. Matsumoto, S. Thomas, G. D. Nguyen, P. R. Forrester, W. Zhao, J. H. Jørgensen, W. R. Dichtel, F. R. Fischer, H. Li, J.-L. Bredas and M. F. Crommie, *Nano Lett.*, 2020, **20**, 963–970.

15 M. Treier, R. Fasel, N. R. Champness, S. Argent and N. V. Richardson, *Phys. Chem. Chem. Phys.*, 2009, **11**, 1209–1214.

16 F. Klappenberger, Y.-Q. Zhang, J. Björk, S. Klyatskaya, M. Ruben and J. V. Barth, *Acc. Chem. Res.*, 2015, **48**, 2140–2150.

17 M. Treier, N. V. Richardson and R. Fasel, *J. Am. Chem. Soc.*, 2008, **130**, 14054–14055.

18 N. A. A. Zwaneveld, R. Pawlak, M. Abel, D. Catalin, D. Gigmes, D. Bertin and L. Porte, *J. Am. Chem. Soc.*, 2008, **130**, 6678–6679.

19 J. F. Dienstmaier, A. M. Gigler, A. J. Goetz, P. Knochel, T. Bein, A. Lyapin, S. Reichlmaier, W. M. Heckl and M. Lackinger, *ACS Nano*, 2011, **5**, 9737–9745.

20 C.-Z. Guan, D. Wang and L.-J. Wan, *Chem. Commun.*, 2012, **48**, 2943–2945.

21 J. F. Dienstmaier, D. D. Medina, M. Dogru, P. Knochel, T. Bein, W. M. Heckl and M. Lackinger, *ACS Nano*, 2012, **6**, 7234–7242.

22 X.-H. Liu, C.-Z. Guan, D. Wang and L.-J. Wan, *Adv. Mater.*, 2014, **26**, 6912–6920.

23 R. Tanoue, R. Higuchi, N. Enoki, Y. Miyasato, S. Uemura, N. Kimizuka, A. Z. Stieg, J. K. Gimzewski and M. Kunitake, *ACS Nano*, 2011, **5**, 3923–3929.

24 S. Lin, J. Gu, H. Zhang, Y. Wang and Z. Chen, *FlatChem*, 2018, **9**, 27–32.

25 D. Toffoli, M. Stredansky, Z. Feng, G. Balducci, S. Furlan, M. Stener, H. Ustunel, D. Cvetko, G. Kladnik, A. Morgante,

A. Verdini, C. Dri, G. Comelli, G. Fronzoni and A. Cossaro, *Chem. Sci.*, 2017, **8**, 3789–3798.

26 G. Zhan, Z.-F. Cai, K. Strutyński, L. Yu, N. Herrmann, M. Martínez-Abadía, M. Melle-Franco, A. Mateo-Alonso and S. D. Feyter, *Nature*, 2022, **603**, 835–840.

27 P. Leidinger and S. Günther, *J. Phys. Chem. C*, 2021, **125**, 12663–12671.

28 M. Salmeron and R. Schlögl, *Surf. Sci. Rep.*, 2008, **63**, 169–199.

29 M. Rößler, P. Geng and J. Wintterlin, *Rev. Sci. Instrum.*, 2005, **76**, 023705.

30 C. T. Herbschleb, P. C. Van Der Tuijn, S. B. Roobol, V. Navarro, J. W. Bakker, Q. Liu, D. Stoltz, M. E. Cañas-Ventura, G. Verdoes, M. A. Van Spronsen, M. Bergman, L. Crama, I. Taminiau, A. Ofitserov, G. J. C. Van Baarle and J. W. M. Frenken, *Rev. Sci. Instrum.*, 2014, **85**, 083703.

31 B. L. M. Hendriksen, S. C. Bobaru and J. W. M. Frenken, *Top. Catal.*, 2005, **36**, 43–54.

32 B. Hendriksen, S. Bobaru and J. Frenken, *Catal. Today*, 2005, **105**, 234–243.

33 B. Hendriksen and J. Frenken, *Phys. Rev. Lett.*, 2002, **89**, 046101.

34 R. Arrigo, M. Hävecker, M. E. Schuster, C. Ranjan, E. Stotz, A. Knop-Gericke and R. Schlögl, *Angew. Chem., Int. Ed.*, 2013, **52**, 11660–11664.

35 S. Axnanda, E. J. Crumlin, B. Mao, S. Rani, R. Chang, P. G. Karlsson, M. O. M. Edwards, M. Lundqvist, R. Moberg, P. Ross, Z. Hussain and Z. Liu, *Sci. Rep.*, 2015, **5**, 9788.

36 D. E. Starr, Z. Liu, M. Hävecker, A. Knop-Gericke and H. Bluhm, *Chem. Soc. Rev.*, 2013, **42**, 5833–5857.

37 F. Tao, M. E. Grass, Y. Zhang, D. R. Butcher, J. R. Renzas, Z. Liu, J. Y. Chung, B. S. Mun, M. Salmeron and G. A. Somorjai, *Science*, 2008, **322**, 932–934.

38 P. Amann, D. Degerman, M.-T. Lee, J. D. Alexander, M. Shipilin, H.-Y. Wang, F. Cavalca, M. Weston, J. Gladh, M. Blom, M. Björkhage, P. Löfgren, C. Schlueter, P. Loemker, K. Ederer, W. Drube, H. Noei, J. Zehetner, H. Wentzel, J. Ahlund and A. Nilsson, *Rev. Sci. Instrum.*, 2019, **90**, 103102.

39 P. Amann, B. Klötzer, D. Degerman, N. Köpfle, T. Götsch, P. Lömker, C. Rameshan, K. Ploner, D. Bikaljevic, H.-Y. Wang, M. Soldemo, M. Shipilin, C. M. Goodwin, J. Gladh, J. Halldin Stenlid, M Börner, C. Schlueter and A. Nilsson, *Science*, 2022, **376**, 603–608.

40 J. Knudsen, T. Gallo, V. Boix, M. D. Strømsheim, G. D'Acunto, C. Goodwin, H. Wallander, S. Zhu, M. Soldemo, P. Lömker, F. Cavalca, M. Scardamaglia, D. Degerman, A. Nilsson, P. Amann, A. Shavorskiy and J. Schnadt, *Nat. Commun.*, 2021, **12**, 6117.

41 R. S. Weatherup, B. C. Bayer, R. Blume, C. Ducati, C. Baehtz, R. Schlögl and S. Hofmann, *Nano Lett.*, 2011, **11**, 4154–4160.

42 L. L. Patera, C. Africh, R. S. Weatherup, R. Blume, S. Bhardwaj, C. Castellarin-Cudia, A. Knop-Gericke,

R. Schloegl, G. Comelli, S. Hofmann and C. Cepek, *ACS Nano*, 2013, **7**, 7901–7912.

43 Y. Fan, K. Nakanishi, V. P. Veigang-Radulescu, R. Mizuta, J. C. Stewart, J. E. Swallow, A. E. Dearle, O. J. Burton, J. A. Alexander-Webber, P. Ferrer, G. Held, B. Brennan, A. J. Pollard, R. S. Weatherup and S. Hofmann, *Nanoscale*, 2020, **12**, 22234–22244.

44 Z.-J. Wang, J. Dong, L. Li, G. Dong, Y. Cui, Y. Yang, W. Wei, R. Blume, Q. Li, L. Wang, X. Xu, K. Liu, C. Barroo, J. W. M. Frenken, Q. Fu, X. Bao, R. Schlögl, F. Ding and M.-G. Willinger, *ACS Nano*, 2020, **14**, 1902–1918.

45 P. R. Kidambi, B. C. Bayer, R. Blume, Z.-J. Wang, C. Baehtz, R. S. Weatherup, M.-G. Willinger, R. Schloegl and S. Hofmann, *Nano Lett.*, 2013, **13**, 4769–4778.

46 M. Stredansky, A. Sala, T. Fontanot, R. Costantini, C. Africh, G. Comelli, L. Floreano, A. Morgante and A. Cossaro, *Chem. Commun.*, 2018, **54**, 3971–3973.

47 F. Haag, P. S. Deimel, P. Knecht, L. Niederegger, K. Seufert, M. G. Cuxart, Y. Bao, A. C. Papageorgiou, M. Muntwiler, W. Auwärter, C. R. Hess, J. V. Barth and F. Allegretti, *J. Phys. Chem. C*, 2021, **125**, 23178–23191.

48 N. Comini, T. Huthwelker, J. T. Diulus, J. Osterwalder and Z. Novotny, *J. Vac. Sci. Technol., A*, 2021, **39**, 043203.

49 L. Trotochaud, A. R. Head, S. Pletincx, O. Karslloğlu, Y. Yu, A. Waldner, L. Kyhl, T. Hauffman, H. Terryn, B. Eichhorn and H. Bluhm, *J. Phys. Chem. B*, 2018, **122**, 1000–1008.

50 K. Severin, *Dalton Trans.*, 2009, 5254–5264.

51 S. Spitzer, A. Rastgoo-Lahrood, K. Macknapp, V. Ritter, S. Sotier, W. M. Heckl and M. Lackinger, *Chem. Commun.*, 2017, **53**, 5147–5150.

52 J. V. Barth, H. Brune, G. Ertl and R. Behm, *Phys. Rev. B: Condens. Matter Mater. Phys.*, 1990, **42**, 9307.

53 D. F. Ogletree, H. Bluhm, G. Lebedev, C. S. Fadley, Z. Hussain and M. Salmeron, *Rev. Sci. Instrum.*, 2002, **73**, 3872–3877.

54 P. Feulner and D. Menzel, *J. Vac. Sci. Technol.*, 1980, **17**, 662–663.

55 V. Pérez-Dieste, L. Aballe, S. Ferrer, J. Nicolàs, C. Escudero, A. Milán and E. Pellegrin, *J. Phys.: Conf. Ser.*, 2013, **425**, 072023.

56 S. Clair, O. Ourdjini, M. Abel and L. Porte, *Chem. Commun.*, 2011, **47**, 8028–8030.